THE JOURNAL OF PHYSICAL CHEMISTRY C

Article

pubs.acs.org/JPCC

Mechanistic Control of the Growth of Three-Dimensional Gold Sensors

Sara Mahshid,[†,§] Adam H. Mepham,[†,§] Sahar Sadat Mahshid,[†] Ian B. Burgess,[†] Tina Saberi Safaei,[‡] Edward H. Sargent,[‡] and Shana O. Kelley*[,†]

[†]Institute of Biomaterials and Biomedical Engineering, University of Toronto, Rosebrugh Building, Room 407, 164 College Street, Toronto, ON M5S 3G9, Canada

[‡]Department of Electrical and Computer Engineering, Faculty of Engineering, University of Toronto, 10 King's College Road, Toronto, ON M5S 3G4, Canada

ABSTRACT: Three-dimensional (3D) electrodes with large surface areas are highly effective biomolecular sensors. These structures can be generated via the electrodeposition of gold inside microscale apertures patterned on the surface of a microelectronic chip. Such electrodes enable the ultrasensitive analysis of nucleic acids, proteins, and small molecules. Since the performance of these electrodes is directly related to their surface area, the ability to control their microscale morphology is critical. Here, we explore an electrochemical model based on the theory of nucleation and growth to better understand how to control the morphology of these electrodes. The insights gained from this model enabled us to create preferential conditions for the formation of different morphological features. We demonstrate for the first time that electrodeposition of 3D nanostructured microelectrodes inside a microscale aperture is governed by two stages of nucleation and growth. The first stage involves the creation of primary nuclei at the bottom of the aperture. The second stage features the generation of new nuclei upon exposure to the bulk solution. Depending on the overpotential, the deposition is then continued by either rapid growth of the original nuclei or fast growth of new nuclei. Faster electrodeposition at high overpotentials promotes directional growth, generating spiky structures. More isotropic growth is observed with low overpotentials, generating rounder features. Ultimately we determine the efficiency of DNA hybridization on a variety of structures and identify the optimal morphologies for rapid DNA–DNA duplex formation.

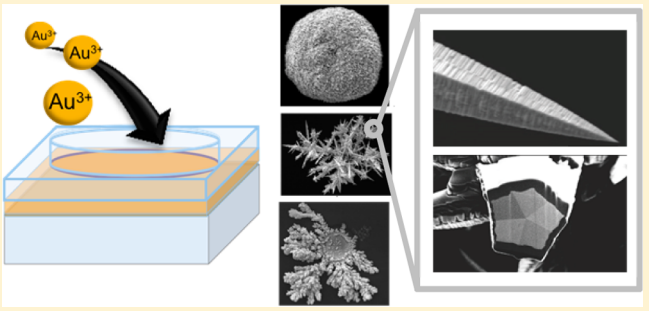

INTRODUCTION

Engineering three-dimensional (3D) structures on the micro- and nanometer scales is of importance for the production of high-performance materials for electronics and biological applications.[1−5] Bottom-up fabrication via self assembly lends itself to the creation of complex 3D architectures in a variety of material systems.[6−9] This approach relies on minimal direct control, relying instead on pattern formation on the basis of thermodynamic equilibria or instabilities.[10] In such a system, the assembly process and the resultant material morphology can be manipulated via any parameters that affect kinetic and thermodynamic properties.[11]

One of the materials that is used extensively for generation of 3D micro- and nanostructures is gold.[12] Gold structures exhibit a variety of morphologies depending on the method of synthesis.[13] Furthermore, 3D gold structures are outstanding candidates for electrochemical biosensing applications[14] and catalyze a number of important chemical reactions.[15,16] The specificity of catalysis and the degree to which the reaction rates are amplified can be linked directly to the morphological properties of 3D gold structures.[17]

Moreover, the crystal structure of gold is also important in determining its performance as a sensor or catalyst. Different crystal facets of gold promote distinct interactions with molecular substrates and targets.[18] Thus, the capacity to modulate the chemical reactivity of different facets during the assembly process is advantageous for the design of optimized structures. As such, methods that control the number and orientation of grain boundaries are of significant interest.

A variety of methods have been used to synthesize gold structures, including sputtering, e-beam lithography, and chemical and electrochemical approaches.[19−22] Although each of these methods has its advantages, none offers access to the suite of synthetically accessible parameters that are available with electrochemical synthesis.[22]

We have previously developed electrodeposited, 3D gold microelectrodes and found that they represent a promising

Special Issue: Richard P. Van Duyne Festschrift

Received: May 22, 2016
Revised: July 16, 2016
Published: July 21, 2016

DOI: 10.1021/acs.jpcc.6b05158
J. Phys. Chem. C 2016, 120, 21123−21132

platform for electrochemical biomolecular detection.[23−28] By creating sensors with large surface areas that protrude into solution, collisional frequencies for biomolecular targets are enhanced.[24] Also, the electrochemical currents generated by these structures are amplified due to the efficient transport of redox-active reporters via radial diffusion.[25] We have further demonstrated that the introduction of nanostructured roughness on the surface of these microelectrodes enhances their biosensing performance.[26] While this system has been applied successfully to the detection of cancer biomarkers,[27] infectious pathogen identification,[23] and organ transplant assessment,[28] we know little about how the 3D features of these sensors influence their performance.

Here, we explore the growth mechanism of 3D gold microsensors and identify factors that enable precise control of morphology and crystallinity. We demonstrate that by changing the gold ion concentration, we can preferentially grow different structures and control directional growth of spiky structures. By increasing the viscosity of the electrolyte solution, we can suppress the growth and generate finer spiky structures. Additionally, by increasing the deposition overpotential, we can also generate finer spiky structures through promoting multiple nucleation and rapid growth of the nuclei clusters. The collection of these parameters enables a high degree of control over the microscale morphology and crystallinity of gold assemblies. We further explore the effects of voltage in more depth to visualize processes related to three-dimensional nucleation and diffusion-controlled growth.[29,30] We ultimately investigate the efficiency of hybridization of DNA duplexes on the surfaces of sensors with differing morphologies and identify the optimal morphology for this type of application. The most effective sensors are generated with high growth-to-nucleation ratios during electrodeposition.

EXPERIMENTAL METHODS

Chip Fabrication. Gold-coated glass wafers (with chrome adhesion layer and positive photoresist coating) were purchased from Telic Company (Valencia, CA). Gold was patterned to create a series of seven leads using standard lithography of the photoresist followed by etching of the gold and chrome layers. Negative photoresist (SU-8 2002) was applied by spin coating and developed using photolithography to create single 10 μm apertures on each lead.

Electrodeposition. Electrodeposition of 3D microelectrodes was performed with a BASI Epsilon potentiostat in dc voltammetry mode. A three-electrode setup was employed with voltage measured relative to an Ag/AgCl reference electrode, and a platinum wire was used as the counter electrode. The deposition time was adjusted for each particular structure in order to keep the quantity of deposited gold roughly constant (i.e., the total coulombs of charge transferred). For the concentration series, the solution was between 1 mM and 500 mM $HAuCl_4$ in a 0.5 M HCl supporting electrolyte. The voltage applied was 0 mV relative to Ag/AgCl. At 50 mM, the time of deposition was 100 s and other deposition times were adjusted accordingly. For the voltage series, the concentration of $HAuCl_4$ was 50 mM and the voltage was varied from +500 mV to −700 mV. For the viscosity series glycerol was added to between 0% and 75% v/v (HCl final concentration was maintained at 0.5 M), with the voltage set to 0 mV and the $HAuCl_4$ concentration maintained at 50 mM.

The surface area of 3D microelectrodes was calculated by measuring the area of the Au reduction peak (~0.80 V vs Ag/AgCl) in 10 mM H_2SO_4 solution. The cyclic voltammetry studies were carried out in the range of 0−1.5 V, and the reduction charge was obtained by integrating the reduction peak. The result was then divided by 500 μC/geometric cm^2 to obtain a geometric estimation of the surface area.[31]

Surface Characterization. Scanning electron microscopy (SEM) images were acquired on a Quanta FEG 250 ESEM. The instrument was used in the high vacuum mode, with typical parameters being 10 kV bias and a 2.5 nm spot size. Magnifications between 1000× and 50 000× were employed. Focused ion beam (FIB) imaging was performed using the Hitachi nanoDUE'T NB5000. Samples were first grounded using a thin layer of silver paste. A thin layer of protective tungsten was then applied to the area of interest using the machine's built-in deposition capacity. Sectioning was performed using high-energy ions to reveal a cross section of the structure. SEM imaging was then done using the built-in SEM module.

Nucleation and Growth Model. The study of electrochemical three-dimensional nucleation processes involved correlating the current to the number of clusters on the electrode surface.[29,30,32−35] As the nucleation rate per active site on the surface, A, and the number density of active sites for nucleation, N_0, vary with overpotential of deposition, the potentiostatic current transients establish the relationship between deposition overpotential and the kinetics of nucleation:[29,30]

$$i = \left(\frac{zFD^{1/2}c}{\pi^{1/2}t^{1/2}}\right)(1 - \exp\{-N_0\pi kD[t - (1 - e^{-At})/A]\}) \quad (1)$$

where i is the current density; z, distance normal to the plane; F, the Faraday constant; D, diffusion coefficient; c, bulk concentration; t, time; N_0, number density of active sites; k, dimensionless constant for growth rate of diffusion zones.

Considering the i_m as the maximum current taking place at t_m, eq 1 can be presented in a dimensionless form by simply plotting i^2/i_m^2 vs t/t_m for different values of the dimensionless parameter $\alpha = N_0\pi kD/A$. The two extreme forms of nucleation are defined for small α or fast nucleation on a limited number of active sites, "instantaneous" nucleation, and large α or slow nucleation on a large number of active sites, "progressive" nucleation.

Electrode Functionalization. Thiolated-DNA strands (0.1 mM) were incubated with TCEP (10 mM) for 1 h to reduce the disulfide bonds. The solution was then diluted to 100 nM PBS 1×, pH 7.0. Glass chips having a set of seven microelectrodes were incubated in 100 μL of 100 nM solutions of thiolated strands overnight. Chips were then rinsed with DI water and incubated in 100 μL of 3 mM MCH in buffer for another 3 h to displace nonspecifically adsorbed DNA and passivate the remaining electrode area. After thoroughly rinsing with DI water, chips were stored in buffer. The thiolated strand surface density (i.e., the number of DNA molecules per unit area of the surface) was determined to be ~6×10^{12} strands/cm^2 by measuring peak current.[36]

Sensor Measurements. Electrochemical measurements were performed at room temperature using an EmStatMUX potentiostat multiplexer (PalmSens Instruments, The Netherlands) and a standard three-electrode configuration containing a platinum counter electrode wire, Sigma-Aldrich and an Ag/AgCl (3 M NaCl) reference electrode (CHI). Experimental

DOI: 10.1021/acs.jpcc.6b05158
J. Phys. Chem. C 2016, 120, 21123−21132

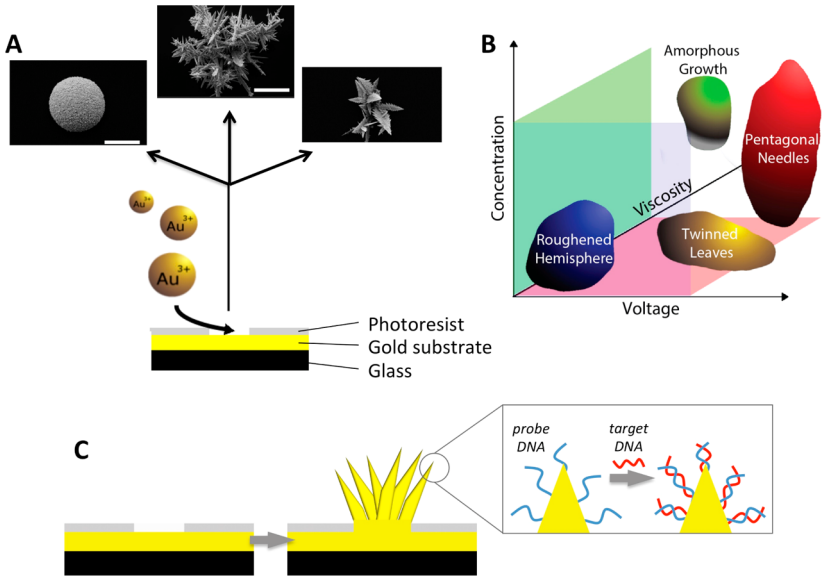

Figure 1. (A) Gold 3D microelectrodes are grown using electrodeposition on a gold substrate with 10 μm apertures as a template. In this study, we explore parameters that could generate different sensor morphologies to determine the optimal properties for biomolecular detectors. (B) The parameters of gold ion concentration, solution viscosity, and applied voltage are varied to explore which regions encourage the growth of particular morphologies. (C) 3D microsensors are tested for DNA hybridization. Blue strand: capture probe that promotes sequence-specific binding of a target sequence. Red: Target DNA strand complementary to probe. Target binding can then be read out using redox-active reporters.[24]

data were collected using square wave voltammetry from −0.05 to −0.45 V in increments of 0.001 V vs Ag/AgCl, with an amplitude of 50 mV and a frequency of 60 Hz. Peak currents were fitted using the manual fit mode in the PSTrace software (PalmSens). All measurements were taken immediately after adding the reagents to the solution (100 nM of signaling strands) to measure the kinetics of hybridization.

RESULTS AND DISCUSSION

Our approach to generating 3D microelectrodes using gold electrodeposition benefits from micropatterned apertures fabricated via photolithography on the surface of a glass chip. A schematic outlining the system used in this study is shown in Figure 1; the application of this microelectrode system for the analysis of specific DNA sequences is also depicted. The electrodeposition is carried out on a glass wafer coated with a thin layer of gold, which is topped with a passivating layer of SU-8 photoresist (Figure 1A). The small (10 μm) apertures in this passivating layer expose the gold substrate to the electrolyte solution, allowing for localized deposition of gold structures. This template-based approach allows for a hemispherical diffusion pattern on top of the aperture that facilitates rapid growth and the faster emergence of structural features compared to the growth achieved on larger planar surfaces.

The three major parameters explored in this study are the concentration of gold ions ($AuCl_4^-$), the viscosity of the electrolyte solution, and the applied voltage. The concentration of gold ions plays a critical role in the kinetics and thermodynamics of the transition from a dissolved state to a solid state. Higher concentrations increase the capacity of the system to transfer sufficient quantities of gold to the growing deposit and enhance electrodeposition kinetics. Viscosity affects the kinetics of the deposition reaction by impeding replenishment of fresh gold ions. Applied voltage controls the relative energies of the solid and dissolved states of gold. As the potential of the cathode is made increasingly negative, the reduction of gold ions to metallic gold becomes more favorable. By varying these three parameters, a phase space is generated featuring regions with different growth regimes and different morphologies (Figure 1B).

For applications where dilute diffusible molecular targets like DNA are being detected (Figure 1C), it is critical to precisely control the morphology and surface area, as both factors influence collisional frequencies as well as binding affinities. To control the formation of 3D structures generated via gold electrodeposition, it is important to understand the influence of nucleation and growth processes. We therefore not only investigate the influence of solution parameters on 3D sensor electrodeposition but also investigate the mechanism of nucleation/growth and seek to link it to the geometrical properties of the resultant structures.

Effects of Solution Conditions of 3D Nanostructured Microelectrode Growth. The effects of varying the concentration and viscosity of the electrolyte solution are shown in Figure 2A and Figure 2B. For each condition, a pair of SEM images are shown at a low (5000×) and high (50 000×) magnification. This allows for the elucidation of changes in the structure at two different scales; both the microscale, so that the overall shape of the structure can be evaluated, and the nanoscale, which allows a detailed analysis of the morphological changes.

The first parameter explored was the concentration of the gold solution (Figure 2A). A wide range of concentrations were tested, ranging from 1 mM to 500 mM, with a roughly logarithmic distribution (each sample approximately 3× more concentrated than the previous). The different concentrations produced at least three qualitatively different growth modes. At the lowest concentration tested (1 mM), the overall morphology features a rounded structure containing a number of distinct lobes on the order of 20−30 μm in size. A study of the surfaces of these structures reveals that the gold assumes a propensity toward nanoscale spikelike structures and is highly porous.

DOI: 10.1021/acs.jpcc.6b05158
J. Phys. Chem. C 2016, 120, 21123−21132

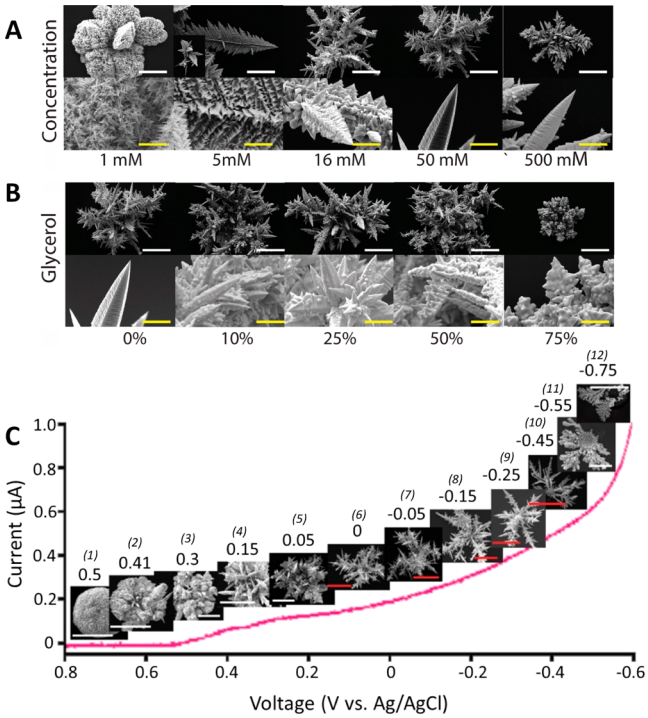

Figure 2. Effects of concentration, viscosity, and voltage on electrodeposition of gold microsensors are studied using scanning electron microscopy (SEM). (A) SEM images for structures generated with varied concentrations of gold ions. Varying the concentration of gold reveals a number of different morphologies. A low (1 mM) concentration produces nanoscale spikelike structures, whereas a 5 mM concentration produces leaflike structures (inset shows structure at 1000× to visualize entire structure) and higher concentrations promote the growth of needles. (B) Increasing viscosity creates rounded structures without visible facets or needles. (C) Increasing deposition potential changes the structures from isotropic rough hemispheres to highly anisotropic structures with a large population of needles. White scale bars are 20 μm, yellow are 2 μm, and red are 40 μm. The potentials used for electrodeposition are displayed above each SEM image and numbered for cross-referencing to Figure 4.

At a 5-fold higher concentration (5 mM) of gold ions, the structure assumes a morphology that is remarkably different from that at 1 mM. Instead of featuring rounded lobes, the structure is dominated by a small number of large leaflike structures. Upon closer inspection at a higher magnification, these structures demonstrate remarkable geometric patterns. Each leaf has a central ridge that runs lengthwise along the middle of the leaf from stem to tip. From this ridge, a number of smaller veins extend. These veins in turn have smaller subveins. This fractal structure indicates that each leaf is either a single crystal domain or a number of domains with fixed relative orientations.

As the gold ion concentration is further increased to 16 mM, a new structural regime is encountered. Leaflike structures are reduced in number, and there appears a new structural feature: needles. At this concentration, the needles are highly ridged, exhibiting a series of peaks and valleys along their length. These needles do not have a consistent cross-sectional shape and appear to be incompletely formed. As the concentration is further increased from 16 mM to 50 and 500 mM, these needles persist. However, at higher concentrations, the ridges are significantly reduced and the needles develop a consistent pentagonal cross section. These needles are of particular interest due to their unique shape, one that has been recognized before in gold structures.[34] Interestingly, higher gold ion concentrations do not necessarily create a greater abundance of needles but rather promote thicker and smoother shapes. As such, the region for creating the greatest number of needles lies in the concentration range between 50 and 500 mM.

In order to change the viscosity of the solution, varying amounts of glycerol were introduced into the solution (Figure 2B). Glycerol was chosen due to its high viscosity and its miscibility in water. As the glycerol concentration is increased, the structures become more compact and dense and the local features are distorted. The sharp edges and facets are replaced with much more rounded features. The most profound change occurs at 75% glycerol. Here, the needles are not present and are replaced with a largely amorphous arrangement that displays weaker directional preference than the highly crystalline material. This experiment indicates that there is another important ingredient for the promotion of needle morphology; namely, low viscosity. The associated high mobility of ions seems integral to allow needles to dominate over largely amorphous, many-grained structures.

The influence of applied potential was initially studied using linear voltammetry (Figure 2C). Variation of applied potential also creates a demonstrable effect on the final morphology (see SEM insets of Figure 2C). At very low overpotentials (+500

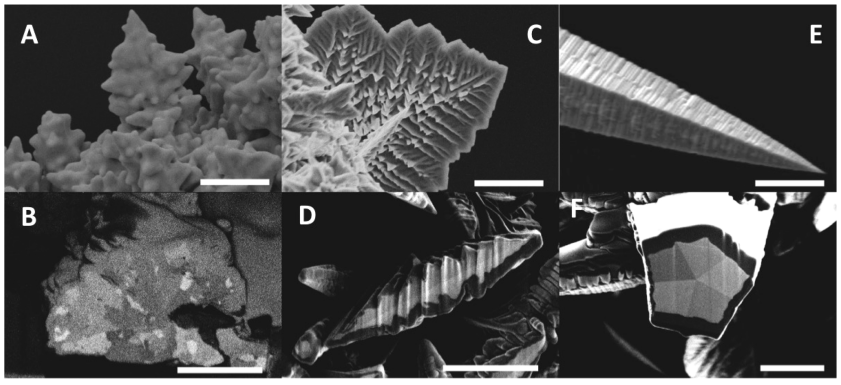

Figure 3. Analysis of the interior structures of electrodeposited gold using FIB. (A, B) The structures generated under high viscosity conditions shows grains with a wide variety of sizes and shapes. (C, D) The leaf structure has a clear crystal twinning about the central plane, indicated by two different shades of gray. (E, F) The needle-like structures have pentagonal cross sections with a 5-fold twinning about the center axis. All scale bars are 2 μm.

DOI: 10.1021/acs.jpcc.6b05158
J. Phys. Chem. C 2016, 120, 21123−21132

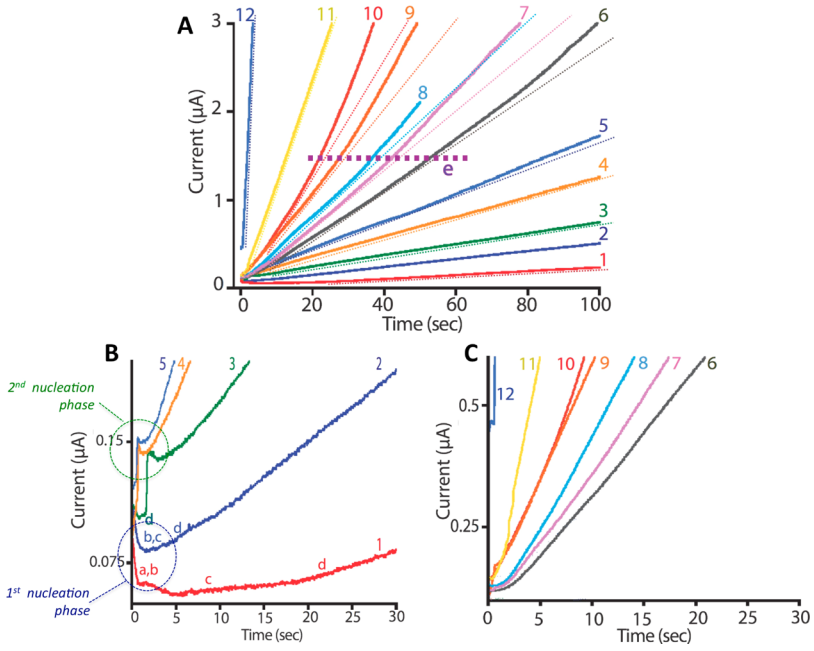

Figure 4. (A) $I-t$ curves for gold electrodeposition within the potential range of +500 to −750 mV. Each trace is labeled with a number that corresponds to a voltage specified in Figure 2. These traces deviate from linearity under certain conditions as shown by the region "e" specified with a dotted line. (B) Electrodeposition data for low-to-moderate overpotentials (500 to 50 mV). (C) Electrodeposition data for higher overpotentials (0 to −750 mV).

mV) the growth is hemispherical overall, with no noticeable anisotropy. At the microscale, the structures are disordered, with a large number of grains of different sizes and orientations. As the magnitude of the potential is increased (i.e., the cathode is made more negative), the structures gain a pronounced anisotropy, with regions of the structure extending farther into the surrounding solution. At a potential of about +150 mV, the needle morphology reemerges, although it is clearly not pentagonal at this voltage and is decorated with a large number of offshoots. Approaching 0 mV, the needles display a full pentagonal geometry. Therefore, to promote the formation of the needles and generate finer spiky structure, a high overpotential (i.e., −250 mV) is needed in addition to a high gold concentration (SEM insets of Figure 2C). It is only in the combinatorial application of these parameters that this particularly interesting morphology becomes the most stable manifestation of gold. Increasing overpotential to more negative values (above −500 mV) causes the spiky structures to be replaced by a flaky morphology with fine structuring.

Images of the exterior of the structures provide insight into the growth mechanism but do not elucidate the extent of crystallinity of the structures. To investigate the internal structures of our 3D sensors more directly, FIB sectioning was performed and SEM images were collected of the resulting cross sections. Using this approach, different crystal grains are revealed within the structures. The structures grown in 75% glycerol are shown in Figure 3A and again in cross section in Figure 3B. In these amorphous structures there is no conserved orientation or direction to the grains. Furthermore, the grains are of vastly different sizes and shapes, with no discernible pattern.

The leaflike structures have a fundamentally different inner morphology than those generated under high viscosity conditions. Figure 3C shows an example of this type of structure displaying a series of veins along its surface and a bilaterally symmetrical shape. A FIB cross section is shown in Figure 3D. Notably, this structure is again composed of multiple grains; however, it has a 2-fold symmetry rather than the disordered arrangement seen previously. This symmetry explains why the top and bottom of the leaf are similar in geometry. This grain boundary is likely a consequence of crystal twinning about a common central plane.[32]

Figure 3E shows a high-resolution SEM image of a well-formed needle. This structure has well-defined facets that are modified by a series of small ridges perpendicular to the length of the needle. FIB sectioning of this structure reveals a clear pentagonal symmetry (Figure 3F). Moreover, this symmetry is seen to stem from a 5-fold arrangement of unique crystal grains about a common center point, with distinct grain boundaries existing between them.

Nucleation and Growth Mechanism of 3D Gold Structures. In most electrodeposition processes, the first phase of structural growth is characterized by rapid nucleation.[29] These nuclei then enter a growth phase, with additional nuclei forming at a reduced rate. As such, crystalline structure is largely established at the time of nucleation. It is apparent from the images presented in Figure 3 that at relatively low concentrations (around 5 mM), nuclei are formed with a 2-fold twinning structure. By contrast, at higher concentrations, there is a shift such that the 5-fold twinned structure is preferable. The appearance of some leaflike structures even at higher concentrations can also be attributed to local depletion of gold ions.

In the case of increased viscosity, the growth rate is severely attenuated relative to the rate of nucleation. Additionally, the geometric entities that represent the lowest energy state under other conditions are no longer preferred, and there is instead a largely random process of deposition. This leads to a loss of directionality that manifests both as an increase in isotropy and a less faceted surface at the local level. Evidently, in order to

DOI: 10.1021/acs.jpcc.6b05158
J. Phys. Chem. C 2016, 120, 21123−21132

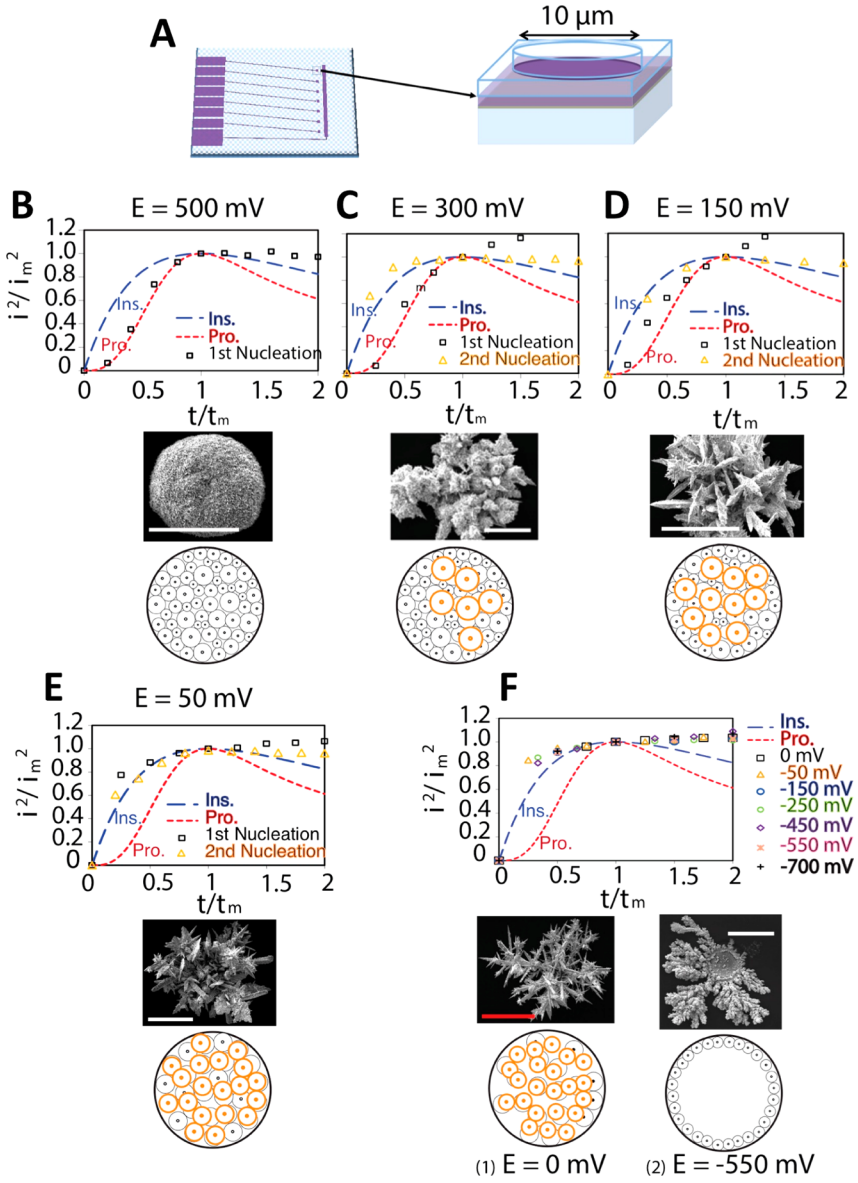

Figure 5. (A) Schematic of the chip-based templates used for electrodeposition, where a 10 μm aperture provides a confined area for the growth of a 3D gold structure. The dimensionless i^2/i_m^2 vs t/t_m responses of microelectrodes electrodeposited at (B) +500, (C) +300, (D) +150, (E) +50, (F1) 0, and (F2) −550 mV and the corresponding theoretical dimensionless models for instantaneous and progressive nucleation. White scale bars are 20 μm, and red scale bars are 40 μm.

promote needle growth, it is critical to create conditions where 5-fold twinned nuclei are the most favorable.

Although FIB imaging provides qualitative insights into the mechanisms of growth, a more comprehensive understanding of this phenomenon was desired. Due to the wide array of different structures that can be produced (bulky, spiky, flaky) within a small window of potentials, we elected to explore the effects of electrodeposition voltage in further depth.

Study of Current–Time (I–t) Transients. The early stage of electrodeposition in our system is associated with a three-dimensional nucleation process, where the number of nuclei and the rate of nucleus formation are strongly governed by the deposition overpotential. We investigated the *I–t* current transients during deposition to establish a relationship between deposition overpotential and the nucleation and growth mechanisms in 3D microelectrodes (Figure 4). During deposition inside the microscale aperture, nucleation and growth are strongly affected by the diffusion of ions around the edges. However, as the deposition proceeds outside the aperture, the geometry of the 3D electrode increases and consequently provides a larger surface for electron transfer over time.

From the *I–t* curves (Figure 4), we can distinguish several deposition phenomena that occur within our microscale apertures. The different phases of growth can be visualized by examining the *I–t* curves generated with low overpotentials, +500 and +400 mV (Figure 4B, curves 1 and 2). The first rise is related to the double-layer formation (region a). A sharp drop in current then occurs due to the depletion of ions following the nucleation process on the planar Au at the bottom of the aperture (region b). Immediately thereafter, steady-state growth fills the aperture (region c). The isotropic growth then proceeds with most of the electrodeposited gold growing outside the aperture and the 3D electrodes expand (region d)

DOI: 10.1021/acs.jpcc.6b05158
J. Phys. Chem. C 2016, 120, 21123–21132

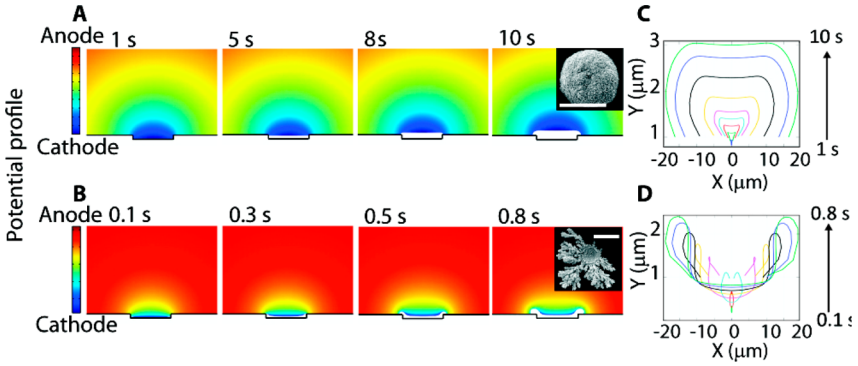

Figure 6. Two-dimensional time-varying simulation results for deposition of Au at (A) +500 mV and (B) −500 mV. The COMSOL geometry consists of an aperture (10 μm wide, 1 μm deep) surrounded by an electrolyte in a 100 μm × 40 μm rectangular space. The electrolyte had a diffusion coefficient of $D = 1 \times 10^{-9}$ m^2/s with initial concentration of $c = 50$ mM. The model is based on a Nernst−Planck equation with electric potential boundary conditions. The simulation results show the deposition front progression from the bottom of the aperture for the minimum and maximum overpotential in our system. At the right, the profiles of deposited layers on the vertical wall of the aperture are shown at (C) +500 mV (top) and (D) −500 mV (bottom). All scale bars are 20 μm.

to form a bulky structure (SEM images 1 and 2 in Figure 2C). When the overpotential is increased to +300, +150, and +50 mV, a sharp rise in the $I-t$ curve is observed at the beginning of region d (Figure 4B, curves 3−5). Here the deposition front undergoes a second nucleation stage, with new nuclei clusters forming on top of the deposit as it confronts the bulk solution outside the aperture. This behavior appears to be responsible for the initiation of needlelike structures in the deposit as shown in the SEM images (5 and 6) of Figure 2C. At more negative potentials (0 to −450 mV), the second nucleation process is gradually merged with the first (Figure 4C, curves 6−12).

Similar types of behavior have been previously reported for metallic structures electrodeposited from microscale/nanoscale pores.[32−35] However, extrapolation of the $I-t$ responses in Figure 4 demonstrates a unique phenomenon in our system related to the deposition of 3D electrodes at higher overpotentials (0 to −450 mV). Within region "e" highlighted in Figure 4, the current traces exhibit a second rise as deposition proceeds beyond 20 s (see curves 6−10). Here, the formation of spiky structures is favored as the rate of elongation of needles is accelerated. At low overpotentials (+300 to +50 mV), the deposition rate controls the growth of deposits. However, at higher overpotentials (0 to −450 mV) where the spikes form, the rate of elongation of these structures is favored.

Analysis of i^2/i_m^2 vs t/t_m. The $I-t$ response curves revealed that two stages of nucleation exist: first, the creation of nuclei on the planar Au at the bottom of the aperture, and second, the generation of new clusters on top of the deposition front caused by exposure to the solution outside of the aperture. The first stage of deposition takes place on a planar electrode located at the bottom of a 10 μm aperture (as shown in Figure 5A). All the area around this planar electrode is made of nonconductive amorphous glass forcing the deposition to initiate at the bottom of aperture.

Figure 5 illustrates the relationship between the deposition overpotential and the nucleation process by comparing current responses in a dimensionless i^2/i_m^2 vs t/t_m plot specified by eq 1. Here, the instantaneous nucleation is compared to progressive nucleation.

At low overpotentials of +500 mV (Figure 5B) and +400 mV (not shown), nucleation follows the progressive model. The low overpotential allows diffusion from the bulk solution into the aperture to readily replenish the consumed ions, resulting in formation of random-size nuclei at all the possible active sites of planar Au (schematic cross section). This results in the formation of the bulky structure shown in the SEM image.

At higher overpotentials such as +300 mV (Figure 5C), after the first stage of nucleation inside the aperture (described by the progressive model), a second nucleation occurs as soon as the deposit is exposed to the bulk solution. This nucleation follows the instantaneous model. The schematic cross section represents the sudden creation of nuclei (orange clusters) on top of the random-sized progressive nuclei (black clusters). This results in the formation of two different microstructures merged together (SEM image of Figure 5C).

Further increases in the overpotential result in a gradual change in the first nucleation stage from progressive to instantaneous, while the second nucleation remains instantaneous. At +150 mV (Figure 5D), a mixture of both the instantaneous and progressive behavior occurs for the first nucleation stage, with the dimensionless current located between the two extreme forms of nucleation. The resulting cross section and the SEM image also show the presence of a bulkier structure underneath, which turns into thick needles as a result of the second instantaneous nucleation (orange clusters in schematic). However, at +50 mV, instantaneous behavior is the only dominant regime in the first and second nucleation stages (Figure 5E). This instantaneous regime in the second nucleation stage promotes a number of smaller nuclei clusters and as a result reduces the thickness of needles in the final morphology.

At negative potentials (0 to −700 mV), the nucleation and growth follows the instantaneous model as shown in Figure 5F. From the SEM images (parts E, F1, and F2 of Figure 5), the deposits tend to have finer needles and the thick ones disappear completely. This is in principle related to the faster nucleation rate on the deposition front, which results in the creation of smaller nuclei on a large number of active sites (Figure 5F1 at 0 mV). The size of nuclei clusters continues to shrink with increasing overpotential. At overpotentials above −450 mV, the possible sites for nucleation appear on the edges and along the wall of the aperture (schematic of Figure 5F2). This results in the formation of a flaky structure.

We used 2D finite-element numerical simulations in COMSOL to model the profile of the deposition front in our

DOI: 10.1021/acs.jpcc.6b05158
J. Phys. Chem. C 2016, 120, 21123−21132

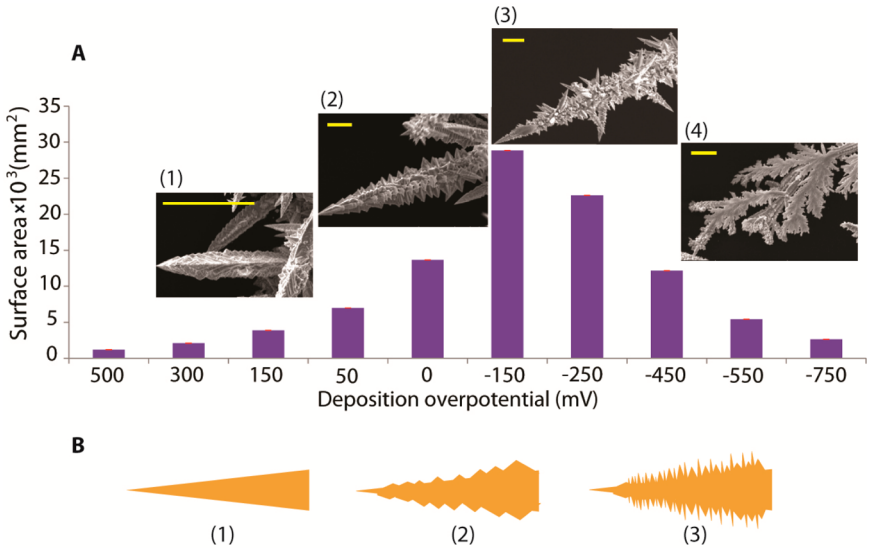

Figure 7. Effect of deposition overpotential on surface nanostructuring. (A) Surface area of 3D structures deposited at different overpotentials (from +500 mV to −750 mV) measured in 50 mM H_2SO_4. Insets: SEM images of structures generated with deposition potentials of (1) +150 mV, (2) 0 mV, (3) −150 mV, (4) −750 mV. (B) Schematic of the individual spikes with different textures deposited in the range of (1) +150 to +50 mV, (2) 0 to −50 mV,(3) −150 to −250 mV. All scale bars are 2 μm.

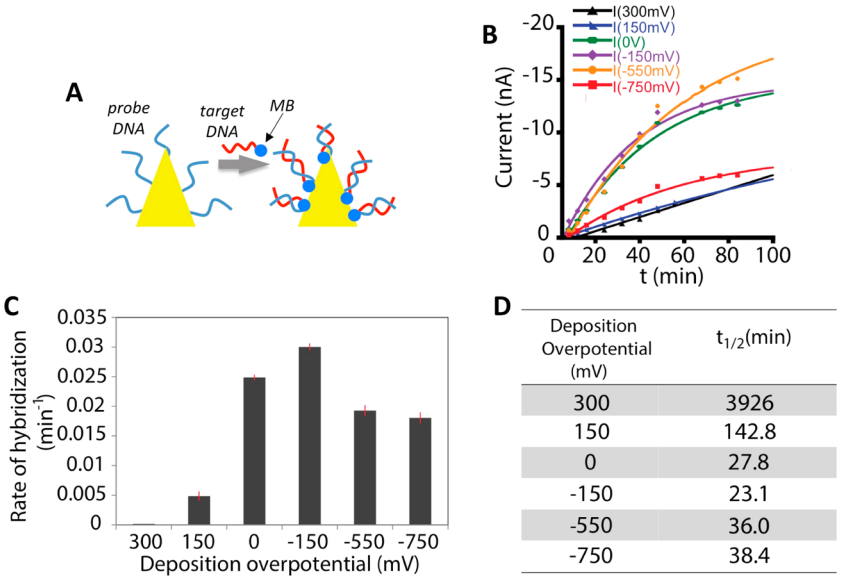

Deposition Overpotential (mV)	$t_{1/2}$(min)
300	3926
150	142.8
0	27.8
-150	23.1
-550	36.0
-750	38.4

Figure 8. (A) DNA detection assay based on 3D gold microsensors. A capture probe (blue) is attached to the sensor. The complementary DNA strand (red) carries methylene blue redox tag (MB) to the electrode surface, which generates an electrochemical signal upon hybridization of DNA strands. (B) Kinetic responses corresponding to DNA−DNA hybridization at sensors deposited with different overpotentials. (C) The hybridization rate and (D) the corresponding $t_{1/2}$ values show the pronounced variation in the efficiency of hybridization induced by different sensor morphologies.

system for both the minimum and maximum overpotentials. The time-series simulation results of Figure 6A reveal the slow progression of the deposition front from the bottom of the aperture and confirm the formation of bulky structures at very low overpotentials (+500 mV). Likewise, Figure 6B demonstrates the deposition profile at −500 mV, where the deposition front moves quickly along the wall of the aperture to the edge. This results in the formation of flaky structures at extreme negative overpotentials. Figure 6C and Figure 6D also demonstrate the profile of the deposit thickness along the vertical wall of the aperture for the bulky and flaky structures, respectively.

Surface Area of Nanostructured 3D Microelectrodes. We also investigated variations in surface area for structures generated with different deposition overpotentials by monitoring cyclic voltammograms generated in sulfuric acid[31] (Figure 7A). We observe that (not surprisingly) the structures generated with low overpotential (+500 mV) exhibit the smallest surface areas (~1200 μm^2). In contrast, spiky structures generated at higher overpotentials boast a much larger surface area. Interestingly, a 3-fold increase is observed for the spiky structures deposited at −150 mV relative to those deposited at +50 mV, despite a similar overall footprint. High-resolution SEM images demonstrate that the needles within these structures have finer nanoscale features that are produced

DOI: 10.1021/acs.jpcc.6b05158
J. Phys. Chem. C 2016, 120, 21123−21132

only at higher overpotentials. This finding is also in accordance with the model proposed in Figure 5, which predicts that increasing the overpotential results in the generation of smaller clusters of nuclei with finer spiky morphology.

As the potential increases above −450 mV, the needles are replaced by fine flakes and the surface area decreases to ∼2600 μm^2 at −750 mV (SEM image, Figure 7A, inset 4). These structures have a different overall morphology, with nucleation occurring on the edge of the aperture followed by planar growth (described in Figures 5 and 6). As a result, fine flakes with smooth texture are formed, limiting surface area.

Study of DNA Hybridization Efficiency on the Surface of 3D Microelectrodes. We compared the efficiency of DNA hybridization on a subset of the structures generated in our mechanistic study. The efficiency and kinetics of DNA hybridization depend strongly on the density and accessibility of DNA probes attached to a surface.[36−38] In general, a higher density of probe strands attached to the surface produces larger signals upon hybridization to redox-tagged complementary strands. However, extremely high probe densities can diminish the rate of hybridization and the efficiency of detection. This is due to the accumulation of more negative charges and the steric hindrance of the populated capturing stands on the surface, which limits the ability of target molecules to easily access and hybridize to their complements.[36]

To investigate the efficiency of DNA hybridization on our 3D sensors, we immobilized a closely packed monolayer of thiolated single-stranded DNA probes on their surface. A complementary DNA strand labeled with methylene blue is then used to monitor the kinetics of hybridization (Figure 8A). The kinetic responses (Figure 8B) and the corresponding rate measurements (Figure 8C) reveal that the rate of DNA−DNA hybridization exhibits a strong dependence on sensor morphology. Spiky structures with finer nanostructuring provide more accessibility for the target hybridization and accelerate the rate of DNA−DNA hybridization. However, on the flaky structures, the rate of hybridization is reduced, likely due to a blocking effect. The structure of the flakes creates hidden sites that may trap probe strands during overnight immobilization but have limited accessibility during the hybridization time. The calculated time $t_{1/2}$ (the time needed for half of the capturing strands to hybridize to signaling strands) is also reported in Figure 8D.

CONCLUSIONS

We conducted a detailed study of the electrodeposition of three-dimensional gold microsensors with varied morphologies. This study revealed the influence of a number of important parameters on the assembly of gold both on a nano- and microscopic scale. This allowed for the customization of parameters to encourage the growth of 5-fold twinned needles which are of particular promise due to their proven utility in biosensing applications. At low overpotentials (+500 to +300 mV) the progressive nucleation and low growth rate encourage the formation of bulky structures. By increasing the overpotential, two discrete stages of nucleation resulted that promoted the creation of spiky structures (+150 to −250 mV). The more instantaneous the nucleation processes (encouraged by higher overpotential) are, the finer is the nanostructuring of the spiky structures. At overpotentials above −450 mV, flaky structures are formed as a result of nucleation on the edge of the aperture. In order to understand the importance of morphology in DNA-based biosensing applications, we studied the rate of hybridization on the surface of these electrodes. Optimal structures that promoted highly efficient hybridization kinetics were identified.

AUTHOR INFORMATION

Corresponding Author

*E-mail: shana.kelley@utoronto.ca. Phone: 416-978-8641.

Author Contributions

§S.M. and A.H.M contributed equally.

Notes

The authors declare no competing financial interest.

ACKNOWLEDGMENTS

This project was funded by the Government of Canada through Genome Canada and the Ontario Genomics Institute (Grant OGI-077), the Province of Ontario through the Ministry of Research and Innovation (ORF-GAPP), and the Natural Sciences and Engineering Research Council of Canada (Discovery Grant).

REFERENCES

(1) Valiev, R. Materials Science: Nanomaterial Advantage. *Nature* **2002**, *419*, 887−889.

(2) Wang, J. Nanomaterial-Based Electrochemical Biosensors. *Analyst* **2005**, *130*, 421−426.

(3) Rose, M.; Korenblit, Y.; Kockrick, E.; Borchardt, L.; Oschatz, M.; Kaskel, S.; Yushin, G. Hierarchical Micro- and Mesoporous Carbide-Derived Carbon as a High-Performance Electrode Material in Supercapacitors. *Small* **2011**, *7*, 1108−1117.

(4) Gittens, R. A.; Olivares-Navarrete, R.; Cheng, A.; Anderson, D. M.; McLachlan, T.; Stephan, I.; Geis-Gerstorfer, J.; Sandhage, K. H.; Fedorov, A. G.; Rupp, F.; et al. The Roles of Titanium Surface Micro/nanotopography and Wettability on the Differential Response of Human Osteoblast Lineage Cells. *Acta Biomater.* **2013**, *9*, 6268−6277.

(5) Potyrailo, R.; Naik, R. R. Bionanomaterials and Bioinspired Nanostructures for Selective Vapor Sensing. *Annu. Rev. Mater. Res.* **2013**, *43*, 307−334.

(6) Noorduin, W. L.; Grinthal, A.; Mahadevan, L.; Aizenberg, J. Rationally Designed Complex, Hierarchical Microarchitectures. *Science* **2013**, *340*, 832−837.

(7) Grinthal, A.; Kang, S. H.; Epstein, A. K.; Aizenberg, M.; Khan, M.; Aizenberg, J. Steering Nanofibers: An Integrative Approach to Bio-Inspired Fiber Fabrication and Assembly. *Nano Today* **2012**, *7*, 35−52.

(8) Phillips, K. R.; Vogel, N.; Hu, Y.; Kolle, M.; Perry, C. C.; Aizenberg, J. Tunable Anisotropy in Inverse Opals and Emerging Optical Properties. *Chem. Mater.* **2014**, *26*, 1622−1628.

(9) Akdim, B.; Pachter, R.; Naik, R. R. Self-Assembled Peptide Nanotubes as Electronic Materials: An Evaluation from First-Principles Calculations. *Appl. Phys. Lett.* **2015**, *106*, 183707.

(10) Pacholski, C.; Kornowski, A.; Weller, H. Self-Assembly of ZnO: From Nanodots to Nanorods. *Angew. Chem., Int. Ed.* **2002**, *41*, 1188−1191.

(11) Whitesides, G. M.; Grzybowski, B. Self-Assembly at All Scales. *Science* **2002**, *295*, 2418−2421.

(12) Jasuja, K.; Berry, V. Implantation and Growth of Dendritic Gold Nanostructures on Graphene Derivatives: Electrical Property Tailoring and Raman Enhancement. *ACS Nano* **2009**, *3*, 2358−2366.

(13) Grzelczak, M.; Pérez-Juste, J.; Mulvaney, P.; Liz-Marzán, L. M. Shape Control in Gold Nanoparticle Synthesis. *Chem. Soc. Rev.* **2008**, *37*, 1783−1791.

(14) Woo, S. M.; Gabardo, C. M.; Soleymani, L. Prototyping of Wrinkled Nano-microstructured Electrodes for Electrochemical DNA Detection. *Anal. Chem.* **2014**, *86*, 12341−12347.

(15) Hashmi, S. K.; Hutchings, G. J. Gold Catalysis. *Angew. Chem., Int. Ed.* **2006**, *45*, 7896−7936.

DOI: 10.1021/acs.jpcc.6b05158
J. Phys. Chem. C 2016, 120, 21123−21132

(16) Liu, M.; Pang, Y.; Zhang, B.; De Luna, P.; Voznyy, O.; Xu, J.; Zheng, X.; Dinh, C. T.; Fan, F.; Cao, C.; et al. *Nature* **2016**, in press.
(17) Campbell, C. T. The Active Site in Nanoparticle Gold Catalysis. *Science* **2004**, *306*, 234−235.
(18) Ming, T.; Feng, W.; Tang, Q.; Wang, F.; Sun, L.; Wang, J.; Yan, C. Growth of Tetrahexahedral Gold Nanocrystals with High-Index Facets. *J. Am. Chem. Soc.* **2009**, *131*, 16350−16351.
(19) Golan, Y.; Margulis, L.; Rubinstein, I. Vacuum-Deposited Gold Films. I. Factors Affecting the Film Morphology. *Surf. Sci.* **1992**, *264*, 312−326.
(20) Lin, Y.; Zou, Y.; Mo, Y.; Guo, J.; Lindquist, R. G. E-Beam Patterned Gold Nanodot Arrays on Optical Fiber Tips for Localized Surface Plasmon Resonance Biochemical Sensing. *Sensors* **2010**, *10*, 9397−9406.
(21) Zhao, P.; Li, N.; Astruc, D. State of the Art in Gold Nanoparticle Synthesis. *Coord. Chem. Rev.* **2013**, *257*, 638−665.
(22) Cherevko, S.; Chung, C. H. Direct Electrodeposition of Nanoporous Gold with Controlled Multimodal Pore Size Distribution. *Electrochem. Commun.* **2011**, *13*, 16−19.
(23) Soleymani, L.; Fang, Z.; Sargent, E. H.; Kelley, S. O. Programming the Detection Limits of Biosensors through Controlled Nanostructuring. *Nat. Nanotechnol.* **2009**, *4*, 844−848.
(24) Soleymani, L.; Fang, Z.; Lam, B.; Bin, X.; Vasilyeva, E.; Ross, A. J.; Sargent, E. H.; Kelley, S. O. Hierarchical Nanotextured Microelectrodes Overcome the Molecular Transport Barrier to Achieve Rapid, Direct Bacterial Detection. *ACS Nano* **2011**, *5*, 3360−3366.
(25) Soleymani, L.; Fang, Z.; Sun, X.; Yang, H.; Taft, B. J.; Sargent, E. H.; Kelley, S. O. Nanostructuring of Patterned Microelectrodes to Enhance the Sensitivity of Electrochemical Nucleic Acids Detection. *Angew. Chem., Int. Ed.* **2009**, *48*, 8457−8460.
(26) Bin, X.; Sargent, E. H.; Kelley, S. O. Nanostructuring of Sensors Determines the Efficiency of Biomolecular Capture. *Anal. Chem.* **2010**, *82*, 5928−5931.
(27) Fang, Z.; Soleymani, L.; Pampalakis, G.; Yoshimoto, M.; Squire, J. A.; Sargent, E. H.; Kelley, S. O. Direct Profiling of Cancer Biomarkers in Tumor Tissue Using a Multiplexed Nanostructured Microelectrode Integrated Circuit. *ACS Nano* **2009**, *3*, 3207−3213.
(28) Sage, A. T.; Besant, J. D.; Mahmoudian, L.; Poudineh, M.; Bai, X.; Zamel, R.; Hsin, M.; Sargent, E. H.; Cypel, M.; Liu, M.; et al. Fractal Circuit Sensors Enable Rapid Quantification of Biomarkers for Donor Lung Assessment for Transplantation. *Sci. Adv.* **2015**, *1*, e150041.
(29) Scharifker, B.; Hills, G. Theoretical and Experimental Studies of Multiple Nucleation. *Electrochim. Acta* **1983**, *28*, 879−889.
(30) Scharifker, B. R.; Mostany, J.; Palomar-Pardavé, M.; González, I On the Theory of the Potentiostatic Current Transient for Diffusion-Controlled Three-Dimensional Electrocrystallization Processes. *J. Electrochem. Soc.* **1999**, *146*, 1005−1012.
(31) Das, J.; Kelley, S. O. Protein Detection Using Arrayed Microsensor Chips: Tuning Sensor Footprint to Achieve Ultrasensitive Readout of CA-125 in Serum and Whole Blood. *Anal. Chem.* **2011**, *83*, 1167−1172.
(32) Johnson, C. J.; Dujardin, E.; Davis, S. A.; Murphy, C. J.; Mann, S. Growth and Form of Gold Nanorods Prepared by Seed-Mediated, Surfactant-Directed Synthesis. *J. Mater. Chem.* **2002**, *12*, 1765−1770.
(33) Ghahremaninezhad, A.; Dolati, A. Diffusion-Controlled Growth Model for Electrodeposited Cobalt Nanowires in Highly Ordered Aluminum Oxide Membrane. *ECS Trans.* **2010**, *28*, 13−25.
(34) Hyde, M. E.; Compton, R. G. A Review of the Analysis of Multiple Nucleation with Diffusion Controlled Growth. *J. Electroanal. Chem.* **2003**, *549*, 1−12.
(35) Xia, Y.; Xiong, Y.; Lim, B.; Skrabalak, S. E. Shape-Controlled Synthesis of Metal Nanocrystals: Simple Chemistry Meets Complex Physics? *Angew. Chem., Int. Ed.* **2009**, *48*, 60−103.
(36) Mahshid, S. S.; Camiré, S.; Ricci, F.; Vallée-Bélisle, A. A Highly Selective Electrochemical DNA-Based Sensor That Employs Steric Hindrance Effects to Detect Proteins Directly in Whole Blood. *J. Am. Chem. Soc.* **2015**, *137*, 15596−15599.
(37) Peterson, a W.; Heaton, R. J.; Georgiadis, R. M. The Effect of Surface Probe Density on DNA Hybridization. *Nucleic Acids Res.* **2001**, *29*, 5163−5168.
(38) Nakano, S. I.; Miyoshi, D.; Sugimoto, N. Effects of Molecular Crowding on the Structures, Interactions, and Functions of Nucleic Acids. *Chem. Rev.* **2014**, *114*, 2733−2758.

DOI: 10.1021/acs.jpcc.6b05158
J. Phys. Chem. C 2016, 120, 21123−21132